High power and power density inductive charging system for busses and heavy-duty vehicles

Giuseppe Guidi [1)] Jon Are Suul [1),2)]

1) Sintef Energy Research, Trondheim, Norway

E-mail: giuseppe.guidi@sintef.no

2) Norwegian University of Science and Technology (NTNU), Trondheim, Norway

ABSTRACT: This paper describes the design of the hardware and control systems for a 100 kW wireless power transfer unit intended for high power battery charging. The developed system is suitable for busses, heavy-duty vehicles and small marine vessels, featuring high power density and high efficiency while remaining structurally simple. A power density exceeding 4 kW/kg has been demonstrated for the coil assembly, with a total dc-dc power transfer efficiency of 97% at rated power. Design criteria are given for the resonant coils, including thermal management considerations. The complete power conversion system is also developed, including SiC-based converters and advanced power flow control strategies aimed at maximizing the operating range in terms of coupling and I/O voltages while minimizing the required volt-ampere ratings of the devices and overall system losses. Experimental results are reported, showing that the system is operating according to calculated performances.

KEY WORDS: wireless power transfer, electric bus, heavy-duty vehicles, power electronics.

1. INTRODUCTION

Inductive-based wireless battery charging systems for commercial electric vehicles are starting to appear on the market. Most systems comply with the SAE J2954 standard[(1)] that has been recently released. This standard covers power levels up to 22 kW and the included specifications define a frequency window of operation between 81.38-90.00 kHz. When it comes to higher power levels, no standard has yet been released. The intended high power standard SAE J2954/2 has been under development for several years already but, due to the very diverse nature of vehicle classes and power levels to be covered, no consensus has been reached upon the frequency window(s) to be utilized or to the power levels that should be covered. To date, several proprietary solutions exist for high power inductive charging, with power capability ranging from few hundred kilowatts [(2)-(4)] up to and beyond a MW[(5)]. The systems from [(2), (3)] are designed to be modular, and the highest power levels are achieved by combining several discrete charging pads. In contrast, the systems from [(4), (5)] are based on a single high power charging pad, with [(4)] being specifically intended for road vehicles while [(5)] was designed for marine applications.

As the required amount of power to be transferred is increased, it is necessary to maximize the power density of the charging system both in terms of power-per-surface (kW/m^2) and power-per-weight (kW/kg). To this aim, it is not immediately obvious whether single-pad solutions will be superior to modular ones, as different aspects concurring to power density (electric and magnetic field magnitude, loss distribution, cooling capabilities, etc.) scale differently with size, as discussed in [(6)]. In the scientific literature, several recent examples of high power and power density inductive charging systems have been reported. In [(7),] an experimentally demonstrated 100 kW system with about 200 kW/m^2 and a coil weight of 50 kg is reported. Details of the commercial system from [(2)] are also published in [(8)], revealing about 180 kW/ m^2 with a total coil weight of approximately 25 kg and a power capability of 75 kW. Lately, a novel multiphase concept has been presented in [(9)], featuring a 100kW system with practically demonstrated surface power density as high as 680 kW/m^2 for the ground assembly (GA) and 905 kW/m^2 for the vehicle assembly (VA). For this design, only the weight of copper and ferrite has been reported, with a total of 42.2 and 8.8 kg for GA and VA, respectively. However, the weight and volumes associated with essential parts like aluminum shields and supporting/protecting structures required for actual installation on the ground or on a vehicle are not included.

In this paper, the power density limits of conventional unipolar single-pad designs are further explored. A system intended for 100 kW power transfer is designed, and the performances are assessed

in terms of achieved power density and efficiency as compared to the state of the art. Experimental measurements are presented to validate the proposed concepts.

2. SYSTEM DESCRIPTION

The considered inductive power transfer system has the simple structure shown in Fig.1. Series-Series (SS) compensation is used as it requires the least number of components, which makes it the most promising topology for high power density design. The known issues of power flow controllability are addressed by proper design of the conversion chain and by using the combined voltage/frequency control strategy presented in [9] and briefly discussed in later sections. A configuration requiring a minimal number of components is also assumed for the power electronics converters. The system is fed by a dc source and an H-bridge is used to excite the primary coil (GA). The receiving side (VA) is equipped with a passive rectifier directly connected to the battery terminals.

2.1. System specifications

The main requirement is that the system must be able to continuously transfer at least 100 kW of power at rated conditions. The power level is selected so that the performance can be directly compared to some of the existing high-power systems. For the same reason, a battery voltage up to 750 V, with a nominal value of 700 V is assumed. The system is supposed to operate with airgaps ranging between 100-150 mm, which are similar to the values used to benchmark most of the existing systems. This set of specifications also determine the rated coil current. Assuming equal I/O nominal dc voltages and neglecting losses:

$$I_n = \frac{P_n}{V_{dc,n}} \cdot \frac{\pi}{2\sqrt{2}} \approx 160\,A\,rms \tag{1}$$

The coil assemblies must also include all the necessary enclosures and shielding structures to allow for deployment on a real vehicle without appreciable change of performance.

3. SYSTEM DESIGN

As the input and output voltages are similar, the GA and VA can use the same coil design. This simplifies the implementation and reduce the number of degrees of freedom in the design. A conventional unipolar square coil topology is chosen for its simplicity and because it is believed to have the best potential in terms of achievable power density [11], at least when considering single-phase designs.

Active cooling of the coil assemblies is needed when high power and power density are the main design targets. Liquid cooling is chosen, as it is known to have higher performance

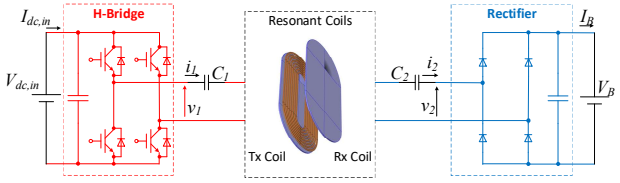

Fig. 1 SS-compensated inductive power transfer system.

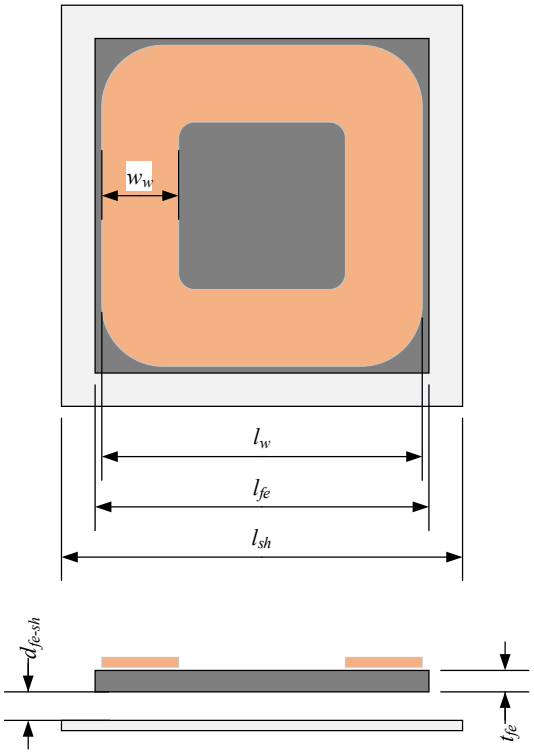

Fig. 2 Basic geometrical parameters for coil optimization.

compared to forced air cooling and because it is assumed to be better suited for the intended applications (heavy-duty vehicles and buses).

3.1. Coil design

When designing square-shaped unipolar coils, the most important variables to be optimized are the external size of the windings l_w and the width of the winding window w_w, as shown in Fig. 2. Both variables have significant impact on the coupling k and the inductance factor A_L, as shown for instance in the normalized graph of Fig.3, for the case of simple symmetrical structures with solid magnetic backplate of same size as the winding ($l_{fe} = l_w$) and with no shielding. Trends are however very similar if slight modifications are introduced in the shape of the ferrite plate and if an aluminum shield is added behind the ferrites.

Using this kind of normalized data, it is possible to calculate a suitable size for the coil pads. The criterion here is that the worst-case coupling in the intended operating range of gap and displacement would remain high enough to limit the reactive

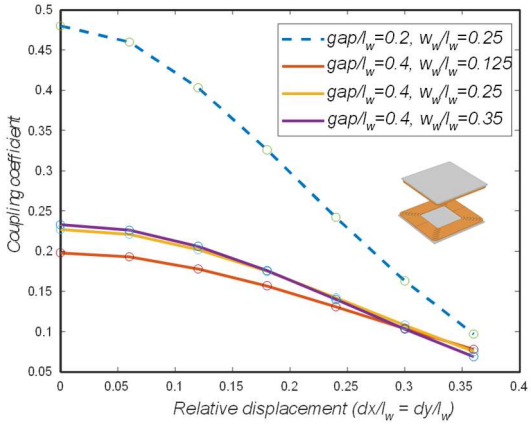

Fig. 3 Variation of coupling coefficient as function of normalized winding size and normalized winding width.

power requirements and the resonant voltages. It was concluded that a pad side length of 500 *mm* would be appropriate.

Once the main size is fixed, k and A_L become just a function of the winding width. Linking w_W to the required number of turns requires information about the Litz-wire diameter, which is determined by the allowed current density J. Here, a compromise must be made between power density and efficiency, taking the thermal constraints into account. After assessing the cooling capabilities, it was decided to aim for a J of about 5 A/mm^2, resulting in a copper cross-section of approximately 30 mm^2 for the Litz-wire. The required number of turns can then be calculated using the power transfer equation of SS-compensated systems:

$$P = \frac{8}{\pi^2} \cdot \frac{V_{dc,in} \cdot V_B}{2\pi f_0 \cdot N^2 \cdot k \cdot A_L} \tag{2}$$

The nominal resonant frequency f_0 has been fixed to 80 kHz, so that it is within the range that will likely be adopted by future standards for such power levels. Once the coil current and the number of turns are known, the thickness of the ferrite plate can be evaluated, taking into account the limits imposed by flux density and losses at the operating frequency. Analytical calculations, corroborated by FEM simulations, suggest that a ferrite thickness of 8 *mm* in the region below the windings is sufficient. Material and cost can however be saved (and power density increased) by reducing the ferrite thickness in areas where the expected flux density is lower. In this case, it was decided to use commercially available 100 mm by 100 mm ferrite tiles with 8 mm thickness for the outermost perimeter and tiles having half the thickness for the inner part. The tile at the center was also omitted, as it contributed very little to the inductance and coupling (see the CAD image in Fig.4).

Other parameters, like the separation distance between winding and ferrite, distance between ferrite and shield, ferrite overhang and extension of the shield, are designed by trading off power density and efficiency. It is imperative that the aluminum plate is extended beyond the ferrite ($l_{sh} > l_{fe}$), so that the fringing field that arises at the edges of the ferrite is properly shielded. A reasonable compromise between covered area and shielding efficiency was found, with l_{sh} = 580 *mm*. The distance between the aluminum shield and the magnetic backplate ($d_{fe\text{-}sh}$) was determined using FEM analysis and experimental data, resulting in $d_{fe\text{-}sh}$ = 20 *mm* as a reasonable compromise. The volume resulting from such separation was used to accommodate the cooling arrangement (heat spreader and cooling plates), as described in the following section. Measured parameters of the coil assemblies are summarized in Table 1.

Table 1 – Measured characteristics of coil assembly

Electrical characteristics	Inductance	37.3 μH (GA, 107 *mm* gap)
		36.8 μH (GA, 147 *mm* gap)
		36.1 μH (VA, 107 *mm* gap)
		35.6 μH (VA, 147 *mm* gap)
	Coupling	0.296 (107 *mm* gap)
		0.207 (147 *mm* gap)
	Q-factor	776 (GA)
		724 (VA)
	Rated current	160 *A rms* (continuous)
Physical characteristics	Planar size	500 x 500 *mm* (w/o shield)
		580 x 580 *mm* (with shield)
	Total thickness	48 *mm*
	Total volume	11 dm^3
	Total weight	24.4 *kg*

One aspect that is important to note is that despite the ideal symmetry that results from the previously described design procedure, the inductances of the two coils are designed to be slightly different. This is to ensure close to ideal zero voltage switching (ZVS) conditions of the H-bridge, as explained in [10]. In practice, the small difference in inductance is achieved by slightly modifying the shape of the innermost turn.

3.2. Thermal management

The water-cooled coil assembly is built according to the layered structure shown in Fig.4. The most important design criterion is the minimization of the thermal resistance of the path from the winding to the heatsinks while maintaining reliable electrical insulation. To this aim, the main insulation barrier between the winding and the ferrite consists of 1 mm-thick thermally conductive aluminum oxide tiles. Good thermal contacts between all layers are secured by using compliant thermal pads, which also

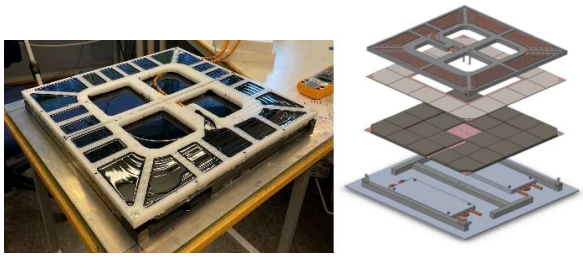

Fig. 4 Complete coil assembly and exploited CAD view.

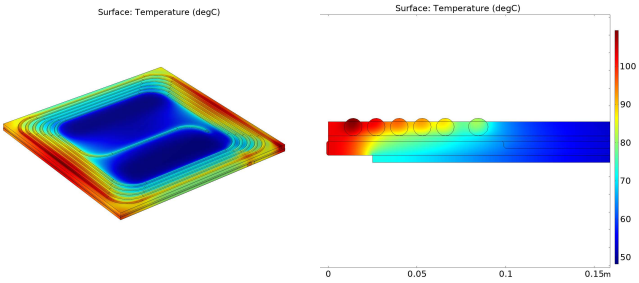

Fig. 5 Steady-state temperature at the rated coil current of 160 A rms at 80 kHz (FEM simulation with 40°C coolant).

constitute an additional isolation barrier. A thermally conductive and rather flexible potting compound (thermal conductivity of 1.1 *W/mK*) is then used to encapsulate the winding and the ferrites, further reducing the thermal resistance and giving structural strength to the assembly. An aluminum heat spreader placed in the region behind the ferrites, and thereby shielded from electromagnetic field, is used to convey the heat towards the cold plates sandwiched between the heat spreader and the main shield.

The cooling performance of the structure has been evaluated with a detailed FEM model (see Fig. 5), showing that the assembly is able to operate continuously at the intended power level. Thermal conductivity of all elements, including Litz-wires, are gathered experimentally, when not directly available from literature. Likewise, heat generation due to losses in windings and ferrite are calculated using measured coil parameters as well as datasheet information related to the magnetic material in use, as discussed in section 4.

3.4. Converter design and control

The H-bridge converter on the GA is built using SiC Mosfet devices rated for 1200 V, 500 A (FF2MR12KM1). For sustained operation at the target frequency of 80 kHz, it is imperative that hard turn-on is avoided. Moreover, even when operating at soft turn-off, the current to be switched must be kept close to zero to avoid excessive losses, as discussed in section 4. This is particularly important for this implementation, since the devices in use are based on conventional 62 mm package that is not optimized for high frequency switching.

The passive rectifier on the VA uses SiC Schottky diode modules (MSC2X101SDA120J), resulting in equivalent device ratings of 1200V, 200 A. The SS-compensation topology of the system ensures that the diode rectifier is soft-switched in all relevant operating conditions.

The design of the coils allows for use of the voltage/frequency control strategy proposed in [10],[12]. Frequency control in the sub-resonant range has been shown to allow for boosting the power transfer at high coupling (transfer distance less than the rated design value of 150 *mm*) while keeping the inverter power factor at the rated value, thus avoiding additional switching losses. As discussed in [13], pulse density modulation (PDM) of the inverter can be used to achieve voltage control, instead of the conventional phase-shift modulation used in [12]. PDM has the advantage of keeping ZVS conditions over the whole voltage control range, thus allowing for sustained operation of the inverter at the rated frequency of 80 kHz while controlling the sending voltage v_1.

4. MODELING AND EVALUATION OF SYSTEM LOSSES

The complete IPT system in Fig.1 includes several loss sources. Within each of the coil assemblies there are losses in the winding, in the magnetic coils, in the resonant capacitor banks, and losses due to induced currents in the metallic structures used for shielding, heat management and structural support. The converters have losses that are conventionally divided into conduction and switching losses. All such loss contributions are analyzed in the following subsections.

4.1 Winding losses

The coils are built using a Litz-wire consisting of 7600 individually insulated strands, each with 0.071 *mm* diameter. Several models exist in literature for the calculation of losses in Litz-wires [14], but none of them can reliably predict the high frequency losses of wires with thousands of insulated strands bundled and twisted according to complex patterns. Detailed FEM simulations are also not feasible due to the extremely complex 3D geometry. After an initial estimation, the equivalent resistance seen at the terminals of the coil assembly has therefore been measured using an LCR meter, resulting in:

$$R_{coil,eq} = 25\,m\Omega\,@\,80\,kHz \tag{3}$$

As the measurement is performed at the terminals of the complete coil assembly using small-signal excitation at the target frequency, the measured resistance includes all loss mechanisms that are linear. Thus, dc and ac losses in the coils (including both

skin-effect and proximity losses), as well as losses due to induced currents in the shields are taken into account.

The dc resistance of the coil was measured to be about 7.5 mΩ. Separate LCR measurements on the wire itself, in a configuration that minimizes external proximity losses gave a wire ac/dc resistance ratio of about 1.9 at 80 kHz. This suggests that the contributions of external proximity losses and of all the shields sum up to about 11 mΩ. Measurements and detailed 3D FEM simulations suggest that the contribution of the aluminum shield is about 7 mΩ, with the rest being external proximity.

4.2 Losses in magnetic material

The LCR measurement cannot be used to assess the losses in the magnetic materials, as they are non-linear and negligible when small-signal excitation is used. Therefore, the losses in the magnetic materials are estimated by using the conventional Steinmetz equation, which is valid for the sinusoidal current flow that is expected in this application. The equivalent resistance of the ferrite plate in a given operating condition is expressed as:

$$R_{fe,eq} = R_{fe,0} \cdot \left(\frac{f[kHz]}{80} \right)^{1.5} \cdot \left(\frac{I_{coil,eq}[A,rms]}{120} \right)^{0.75} \tag{4}$$

Steinmetz parameters are calculated from datasheet of the material in use. The equivalent resistance at 80 kHz and 120 A is estimated using a FEM simulation and integrating Steinmetz formula over the whole volume occupied by the ferrite. It is thus assumed that the flux distribution remains similar for different values of coil current or, in other words, that the relative permeability of the ferrite can be considered reasonably constant over the considered range of excitation.

In (4), the coil equivalent current $I_{coil,eq}$ is used, defined as:

$$\begin{aligned} I_{1,eq} &= \sqrt{\left(I_1 + k \cdot I_2 \cdot \cos\varphi_{1,2}\right)^2 + \left(k \cdot I_2 \cdot \cos\varphi_{1,2}\right)^2} \\ I_{2,eq} &= \sqrt{\left(I_2 + k \cdot I_1 \cdot \cos\varphi_{1,2}\right)^2 + \left(k \cdot I_1 \cdot \cos\varphi_{1,2}\right)^2} \end{aligned} \tag{5}$$

where the angle $\varphi_{1,2}$ is the angular displacement between the phasors of the two coil currents. This definition is introduced to account for the increase of flux density that takes place due to the additional magnetic field produced by the current flowing in the other coil. This contribution becomes important when the coupling is increased and when the system is operated out of resonance, since the two coil currents are no longer in quadrature.

4.3 Losses in resonant capacitors

The equivalent series resistance (ESR) of the resonant capacitor banks was also measured using the same LCR meter used for the coil assembly, resulting in:

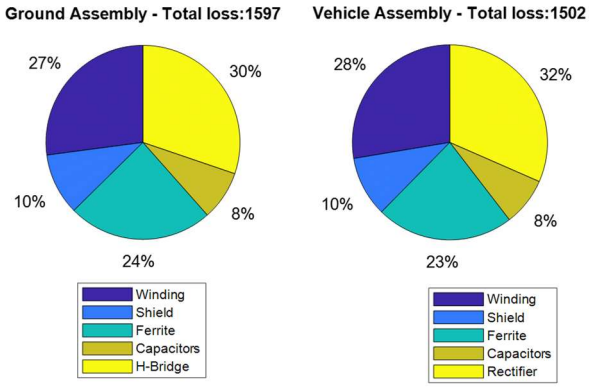

Fig. 6 Estimated loss distribution of the IPT system at rated power flow (100 kW at 700 V) and rated gap (150 *mm*).

$$R_{C,eq} \approx 5m\Omega \,@\, 80kHz \tag{6}$$

4.4 Inverter losses

Conduction losses in the SiC MOSFETs are estimated from datasheet values:

$$R_{ON,MOSFET} \approx 3m\Omega \,@\, T_j = 100°C \tag{7}$$

The system is operated so that only soft turn-off losses are generated. Such losses are estimated from datasheet values by assuming a linear relationship between the turn-off current and the losses. A linear relationship is also assumed between the switching losses and the dc-link voltage:

$$P_{conv,sw} \approx 4 \cdot f[Hz] \cdot \left(6[mJ] \cdot \frac{I_{sw} - 10[A]}{200[A]} \cdot \frac{V_{dc}}{600[V]} \right) \tag{8}$$

4.5 Rectifier losses

Conduction losses in the diode rectifier are estimated using a piecewise linear approximation of the on-state characteristics of the devices. Considering that there are two diodes in parallel on each of the bridge arms, the losses are calculated as:

$$\begin{aligned} P_{rect} &\approx 4 \cdot \left(V_{th} \cdot \frac{I_{2,avg}}{2} + r_d \cdot \left(\frac{I_{2,rms}}{2} \right)^2 \right) \\ V_{th} &= 0.75V, \quad r_d = 10m\Omega \end{aligned} \tag{9}$$

The switching losses can be neglected, due to the sinusoidal shape of the current leading to close to ideal soft-switching of the diodes.

4.6 Calculated system efficiency

Using the expressions (3)-(9) for the loss contributions, the expected efficiency of the system can be calculated in any operating condition. At rated power (100 kW) and rated dc voltage (700 V) at both ends, total losses are estimated as about 3100 W, giving a dc-dc efficiency of about 97%. The estimated loss distribution under rated power flow at the rated gap of 150 mm is reported in Fig. 6.

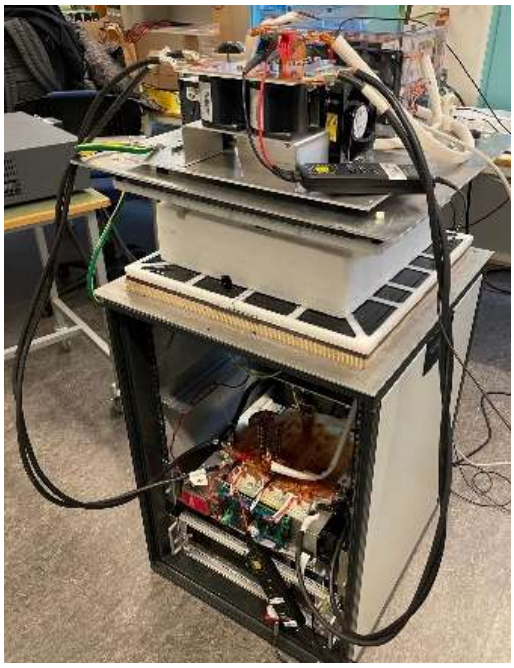

Fig. 7 Experimental setup, including coil assemblies, resonant capacitors, converters.

5. EXPERIMENTAL RESULTS

The complete setup is shown in Fig.7. The system has been tested using a common dc source for both transmitter and receiver, so that only losses need to be supplied. Moreover, with this setup the overall dc-dc losses can be reliably measured.

The first measurements were obtained when changing the dc voltage while operating the inverter in square-wave mode at the rated frequency of 80 kHz. The power drawn from the dc supply, representing the total system losses, was measured together with the power circulated within the system (the output power). Two sets of measurements were taken, corresponding to different airgap distances. Results are reported in Fig. 8, showing a dc-dc system efficiency of 97.0% when the output power is 100.9 kW. A peak efficiency of 97.9% has been recorded when operating at rated voltage and reduced gap, with an output power of 70.6 kW.

Voltage and current waveforms recorded in rated conditions are shown in Fig. 9. It is seen that the inverter operates at slightly inductive output power factor, leading to low switching losses and reduced EMI.

Fig. 10 shows the calculated and measured characteristics of the system for maximum and minimum specified transmission distance. It is seen that frequency regulation allows for operation at rated current (corresponding to about 70 kW at 500 V dc) in the whole range of coupling. The oscilloscope measurements in Fig.11 show that the only noticeable difference between operation at the

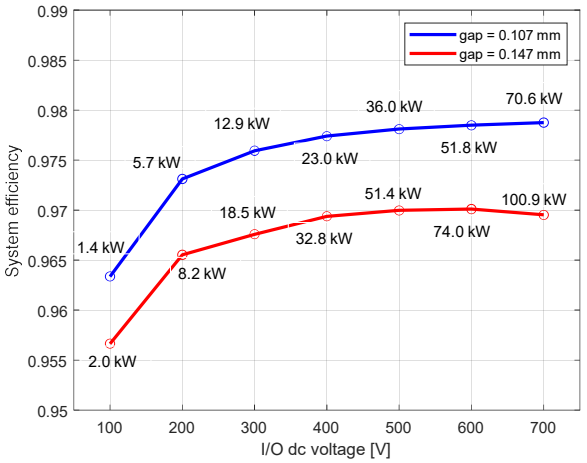

Fig. 8 Measurement of overall system efficiency and output power for different dc voltage and different gap distances.

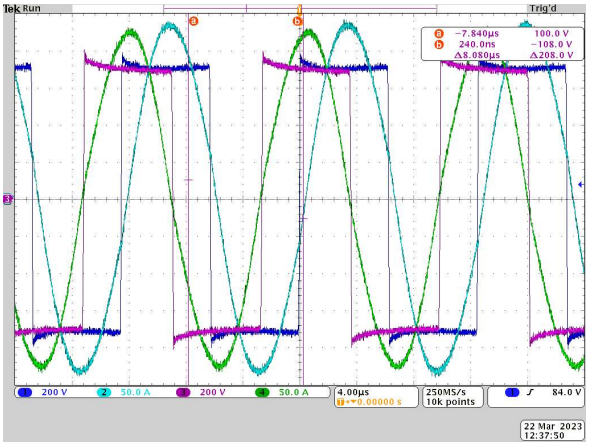

Fig. 9 Experimental waveforms at rated power (100 kW).
Ch1 (blue): GA voltage (200 V/div)
Ch2 (cyan): GA current (50 A/div)
Ch3 (magenta): VA voltage (200 V/div)
Ch4 (green): VA current (50 V/div)

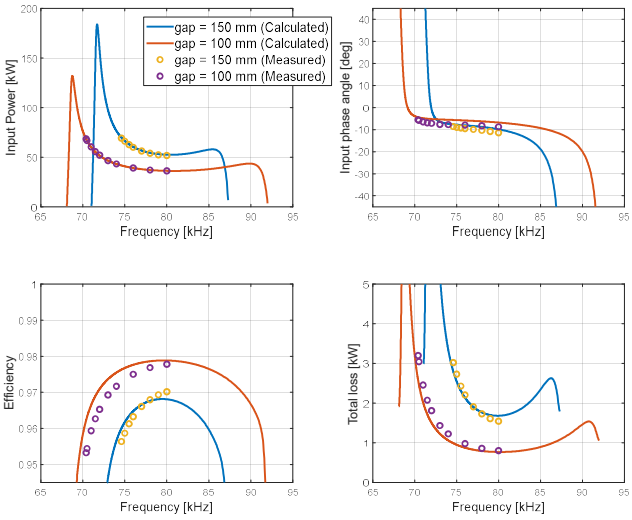

Fig. 10 Comparison of calculated and measured characteristics of the designed system ($V_{in,dc} = V_B = 500\ V$).

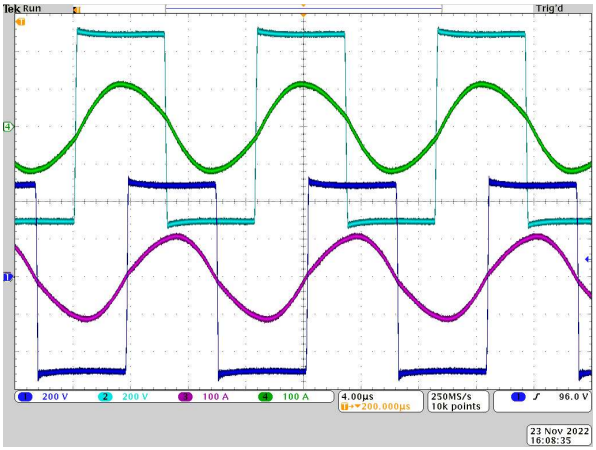

(a) operation at rated frequency, 80 kHz.

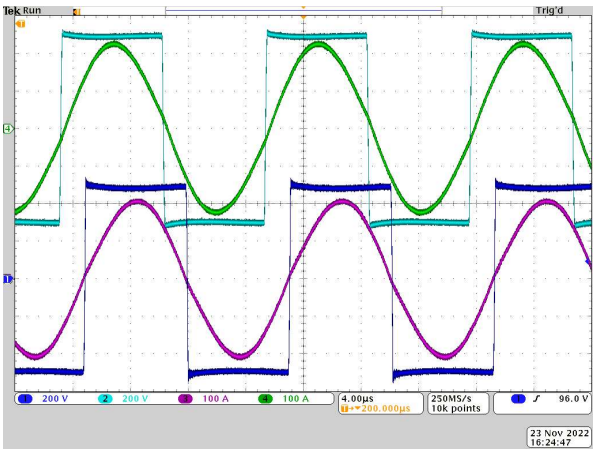

(b) operation at 70.4 kHz, corresponding to rated $I_1 = 160\ A\ rms$

Fig. 11 System operation at $V_{in,dc} = V_B = 500\ V$, gap = $107mm$. Upper waveforms: v_1, i_1; Lower waveforms: v_2, i_2.

rated resonance frequency (80 kHz) and at sub-resonant frequency (70.4 kHz in figure), besides the increased power flow, is the phase displacement between primary and secondary-side quantities. Close to the ideal 90 deg phase difference is seen at the resonant frequency, while the phase difference is reduced as the frequency is lowered. Crucially, though, the output power factor of the inverter remains almost unchanged. Operation is always slightly inductive and is insensitive to both frequency and coupling variations, ensuring optimal ZVS over a wide range of operation.

6. CONCLUSIONS

In this paper, the power density limits of conventional unipolar square coil arrangements for inductive power transfer have been explored. A system capable of delivering 100 kW continuously over a nominal 150 mm gap has been designed, realized and tested.

By careful design of all the elements in the system, including the power converters and the power flow control strategy, the target power flow has been demonstrated with an achieved power density exceeding 4 kW/kg and a surface power density of about 400 kW/m^2. In addition, an efficiency of 97% from the dc input to the dc output has been measured while transmitting the rated power over the rated gap. The efficiency vs. power density trade-off is thus superior to most previously reported systems, when conditions are equalized.

The presented level of performance has been achieved using only off-the-shelf components, without resorting to exotic and/or expensive materials and without using complex manufacturing procedures. This shows that high power inductive charging systems can be used to facilitate electrification of heavy-duty transport and for other energy-sensitive applications where high power must be combined with light weight and small footprint.

ACKNOWLEDGMENT

This work was supported by the Research Council of Norway under Project number 294871 "Ultra-high power density wireless charging for maritime applications" and under Project number 304213 "Research and Demonstration of Key Technologies for Intelligent-connected Electric Vehicles in China and Norway (KeyTech NeVeChiNo)".

REFERENCES

(1) "Wireless Power Transfer for Light-Duty Plug-in/Electric Vehicles and Alignment Methodology, "SAE J2954, 2022-08.

(2) INDUCTEV (formerly Momentum Dynamics) www.inductev.com

(3) ENRX (formerly IPT Technology) https://www.enrx.com/

(4) WAVE – Wireless Advanced Vehicle Charging, www.waveipt.com/

(5) G. Guidi, J. A. Suul, F. Jenset and I. Sorfonn, "Wireless Charging for Ships: High-Power Inductive Charging for Battery Electric and Plug-In Hybrid Vessels," in *IEEE Electrification Magazine*, vol. 5, no. 3, pp. 22-32, Sept. 2017.

(6) G. Guidi, J. A. Suul, "Analysis of Scaling Characteristics for Inductive Power Transfer Coils" in *Proceedings of the International Power Electronics Conference,* IPEC 2022 ECCE Asia, Himeji, Japan, / Hybrid Conference, 15-19 May 2022, 8 pp.

(7) V. P. Galigekere, J. Pries, O. C. Onar, G.-J Su, S. Anwar, R. Wiles, L. Seiber, J. Wilkins, "Design and implementation of an optimized 100kW stationary wireless charging system for EV battery recharging," in *Proceedings of the 2018 IEEE Energy Conversion Congress and Exposition*, ECCE 2018, Portland, Oregon, USA, 23-27 September 2018, pp. 3587-3592

(8) J. M. Miller, A. W. Daga, F, J. McMahon, P. C. Schrafel, B. Cohen, A. W. Calabro, "A Closely Coupled and Scalable High-Power Modular Inductive Charging System for Vehicles," in *IEEE Journal of Emerging and Selected Topics in Power Electronics*, vol. 10, no. 3, pp. 3259-3272, June 2022.

(9) O. C. Onar, G.-J. Su, M. Mohammad, V. P. Galigekere, L. Seiber, C. White, J. Wilkins, R. Wiles, "A 100-kW Wireless Power Transfer System Development Using Polyphase Electromagnetic Couplers," in *Proceedings of the 2022 IEEE Transportation Electrification Conference*, ITEC 2022, Anaheim, California, USA, 15-17 June 2022, pp. 273-278

(10) G. Guidi and J. A. Suul, "Minimizing Converter Requirements of Inductive Power Transfer Systems with Constant Voltage Load and Variable Coupling Conditions," in *IEEE Transactions on Industrial Electronics*, vol. 63, no. 11, pp. 6835-6844, Nov. 2016.

(11) R. Bosshard, U. Iruretagoyena and J. W. Kolar, "Comprehensive Evaluation of Rectangular and Double-D Coil Geometry for 50 kW/85 kHz IPT System," in *IEEE Journal of Emerging and Selected Topics in Power Electronics*, vol. 4, no. 4, pp. 1406-1415, Dec. 2016.

(12) J. Zhou, G. Guidi and J. A. Suul, "High Efficiency operation of Inductive Battery Charging System by the Coordinated Voltage-Frequency Control during Large Variations in Coupling Conditions," in *Proceedings of the 2021 IEEE 12th Energy Conversion Congress & Exposition – Asia*, ECCE-Asia 2021, Singapore, 2021, pp. 2449-2456.

(13) J. Zhou, G. Guidi, K. Ljøkelsøy and J. A. Suul, "Analysis and Mitigation of Oscillations in Inductive Power Transfer Systems with Constant Voltage Load and Pulse Density Modulation," *2021 IEEE Energy Conversion Congress and Exposition* (ECCE), Vancouver, BC, Canada, 2021, pp. 1565-1572.

(14) C. R. Sullivan, R. Y. Zhang, "Analytical Model for Effects of Twisting on Litz-Wire Losses," in *Proceedings of the 2014 IEEE 15th Workshop on Control and Modeling for Power Electronics*, COMPEL 2014, Santander, Spain, 22-25 June 2014, 10 pp